

## RESEARCH ARTICLE SUMMARY

## NEUROSCIENCE

# In vivo multiplex imaging of dynamic neurochemical networks with designed far-red dopamine sensors

Yu Zheng<sup>†</sup>, Ruyi Cai<sup>†</sup>, Kui Wang<sup>‡</sup>, Junwei Zhang<sup>‡</sup>, Yizhou Zhuo, Hui Dong, Yuqi Zhang, Yifan Wang, Fei Deng, En Ji, Yiwen Cui, Shilin Fang, Xinxin Zhang, Haiyun Huang, Kecheng Zhang, Jinxu Wang, Guochuan Li, Xiaolei Miao, Zhenghua Wang, Yuqing Yang, Shaochuang Li, Jonathan B. Grimm, Kai Johnsson, Eric R. Schreiter, Luke D. Lavis, Zhixing Chen, Yu Mu, Yulong Li\*

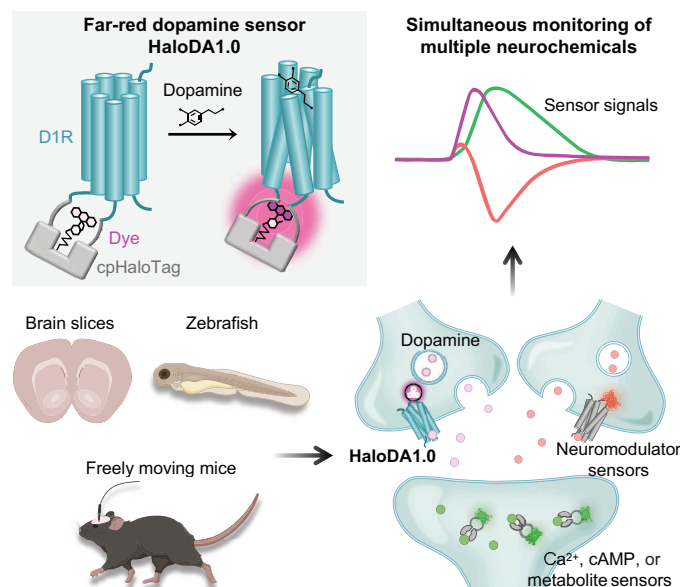


Full article and list of author affiliations: <https://doi.org/10.1126/science.adt7705>

**INTRODUCTION:** Neurochemical signals, including neurotransmitters, neuromodulators, and intracellular signaling molecules, are dynamically modulated within networks that mediate various brain functions and contribute to neurological disorders. Dopamine (DA), one of the most important neuromodulators, interacts intricately with other neuromodulators such as acetylcholine (ACh) and endocannabinoids (eCBs), along with intracellular signals such as cyclic adenosine 5'-monophosphate (cAMP) and  $Ca^{2+}$ . Decoding these networks is crucial for understanding neural mechanisms underlying behaviors and related disorders. However, current genetically encoded sensors are limited to the green and red spectra, hindering real-time simultaneous detection of multiple neurochemical signals. There is an urgent need to expand the spectral range of neuromodulator sensors to include far-red and near-infrared (NIR) wavelengths (i.e., those >650 nm).

**RATIONALE:** By utilizing G protein-coupled receptors (GPCRs) and circularly permuted fluorescent proteins (cpFPs), we and others have developed a series of green and red GPCR activation-based (GRAB) sensors, enabling the detection of neuromodulators in vivo with high spatiotemporal resolution. However, expanding this strategy with far-red/NIR proteins presents challenges because of the suboptimal properties of existing far-red/NIR fluorescent proteins. The combination of protein tags with rhodamine derivatives offers a promising alternative approach, providing a broad spectral range and high brightness. We integrated the cpHaloTag-chemical dye approach with the GRAB strategy, resulting in the creation of HaloDA1.0, the first single protein-based far-red chemigenetic sensor for neuromodulators. Capitalizing on its far-red wavelength, HaloDA1.0 provides opportunities for monitoring three neurochemicals simultaneously by combining with existing green and red sensors.

**RESULTS:** HaloDA1.0 demonstrated robust sensitivity, high specificity, subsecond response kinetics, and compatibility with a variety of far-red chemical dyes. Combining HaloDA1.0 with two other neuromodulator sensors in acute mouse brain slices, we achieved simultaneous imaging of three key neuromodulators, DA, ACh, and eCB, after electrical stimulation and pharmacological interventions. In zebrafish larvae, HaloDA1.0 enabled three-color imaging of DA, ATP, and  $Ca^{2+}$ , revealing coordinated activation patterns during electrical shocks and acute seizure attacks. Our in vivo dye screening further established HaloDA1.0's effective performance in living mice with a silicon-rhodamine dye. This enabled dual-color recording alongside optogenetic manipulations. Furthermore, we achieved simultaneous multicolor recording of spontaneous and behaviorally associated DA, ACh, and cAMP signals in the nucleus accumbens, unveiling distinct regulatory patterns and providing a comprehensive perspective of concurrent regulation of intracellular cAMP signaling.



**Development and applications of a far-red dopamine sensor for simultaneous monitoring of multiple neurochemicals.** This sensor functions by modulating the equilibrium of the lactone form (L) and zwitterionic form (Z) of chemical dyes. Combining the far-red sensor with green and red sensors enables simultaneous monitoring of three neuromodulators or both neuromodulators and intracellular signals in various biological systems. Some schematics were created using BioRender.com.

**CONCLUSION:** To monitor multiple neurochemicals simultaneously, we developed the chemigenetic far-red DA sensor HaloDA1.0, enabling sensitive DA detection both in vitro and in vivo. This sensor demonstrates significant advantages for monitoring multiple neurochemical signals across diverse biological systems, including cultured neurons, acute mouse brain slices, zebrafish, and living mice. This strategy enhances our understanding of the complex interactions among various neurochemical signals, paving the way for deeper insights into neural circuit function and improved comprehension of neurological and psychiatric disorders. □

\*Corresponding author. Email: [yulongli@pku.edu.cn](mailto:yulongli@pku.edu.cn) †These authors contributed equally to this work. ‡These authors contributed equally to this work. Cite this article as Y. Zheng et al., *Science* 388, eadt7705 (2025). DOI: 10.1126/science.adt7705

## NEUROSCIENCE

# In vivo multiplex imaging of dynamic neurochemical networks with designed far-red dopamine sensors

Yu Zheng<sup>1,2,†</sup>, Ruyi Cai<sup>2,3,†</sup>, Kui Wang<sup>4,†</sup>, Junwei Zhang<sup>5,†</sup>, Yizhou Zhuo<sup>2,3</sup>, Hui Dong<sup>2,3</sup>, Yuqi Zhang<sup>3,6</sup>, Yifan Wang<sup>7</sup>, Fei Deng<sup>2,3</sup>, En Ji<sup>2,3</sup>, Yiwen Cui<sup>1,2</sup>, Shilin Fang<sup>4</sup>, Xinxin Zhang<sup>4</sup>, Haiyun Huang<sup>1,2</sup>, Kecheng Zhang<sup>5</sup>, Jinxu Wang<sup>3,8</sup>, Guochuan Li<sup>3</sup>, Xiaolei Miao<sup>3,8</sup>, Zhenghua Wang<sup>1,2</sup>, Yuqing Yang<sup>2,3</sup>, Shaochuang Li<sup>3</sup>, Jonathan B. Grimm<sup>9</sup>, Kai Johansson<sup>6</sup>, Eric R. Schreier<sup>9</sup>, Luke D. Lavis<sup>9</sup>, Zhixing Chen<sup>1,5,10</sup>, Yu Mu<sup>4,11</sup>, Yulong Li<sup>1,2,3,10\*</sup>

Dopamine (DA) plays a crucial role in a variety of brain functions through intricate interactions with other neuromodulators and intracellular signaling pathways. However, studying these complex networks has been hindered by the challenge of detecting multiple neurochemicals in vivo simultaneously. To overcome this limitation, we developed a single-protein chemigenetic DA sensor, HaloDA1.0, which combines a cpHaloTag–chemical dye approach with the G protein–coupled receptor activation–based (GRAB) strategy, providing high sensitivity for DA, subsecond response kinetics, and a far-red to near-infrared spectral range. When used together with existing green and red fluorescent neuromodulator sensors, calcium indicators, cyclic adenosine 5′-monophosphate sensors, and optogenetic tools, HaloDA1.0 showed high versatility for multiplex imaging in cultured neurons, brain slices, and behaving animals, facilitating in-depth studies of dynamic neurochemical networks.

Neuromodulators play an essential role in shaping behavior, in which specific neurons integrate a variety of neuromodulatory inputs to finely tune neural circuits through intracellular signaling mechanisms and pathways (1, 2). The monoamine dopamine (DA) participates in many critical functions, including reward and motivation, learning, and movement (3–5). The multifaceted role of DA in physiology is intricately linked with its interactions with other neuromodulators, including acetylcholine (ACh), endocannabinoids (eCBs), and serotonin (5-HT) (6, 7). Furthermore, the interaction of DA with its receptors triggers intracellular signaling through cytosolic second messengers such as cyclic adenosine 5′-monophosphate (cAMP) and Ca<sup>2+</sup> (8, 9). Therefore, obtaining a comprehensive view of the functions of DA requires precise examination of its intricate interactions within neurochemical networks, including its complex relationship with the other neuromodulators and intracellular signaling molecules with high spatial and temporal resolution.

Achieving this goal requires tools that can be used to simultaneously monitor various neurochemical signals, including multiple neuromodulators and/or a combination of neuromodulators and cytosolic

signaling molecules in vivo. Previously, our group and others developed a series of genetically encoded DA sensors based on the G protein–coupled receptor (GPCR) activation–based (GRAB) strategy, which can be used to visualize DA dynamics in vivo with exceptionally high spatiotemporal resolution (10–14). However, despite their advantages, these fluorescent sensors are limited to the green and red spectra (15), restricting their use to dual-color imaging and limiting our ability to simultaneously track a large number of neurochemical signals. This has led to the urgent need to extend the spectral range of neuromodulator sensors, particularly to include far-red and near-infrared (NIR) wavelengths (i.e., those >650 nm). However, engineering genetically encoded far-red/NIR sensors is challenging due to the relatively low brightness of existing far-red/NIR fluorescent proteins and the difficulty associated with obtaining suitable circularly permuted far-red/NIR fluorescent proteins required for GPCR-based sensors (16, 17).

Combining the dye-capture protein HaloTag (18) with rhodamine derivatives offers a promising alternative approach, providing a broad spectral range, high brightness, and high photostability (19). Similar to green fluorescent protein (GFP), for which the chromophore ionization state is dependent on the surrounding environment (20), rhodamine derivatives are also environment sensitive. They reside in an equilibrium between the closed, nonfluorescent lactone (L) form and the open, fluorescent zwitterionic (Z) form (21, 22). Although this chemigenetic strategy has been used successfully to develop far-red/NIR Ca<sup>2+</sup> and voltage sensors (23, 24), much of these sensors' performance in vivo has not been studied.

Here, we combined our GRAB strategy with chemigenetics to develop a far-red DA sensor called GRAB<sub>HaloDA1.0</sub> (hereafter referred to as HaloDA1.0). We then used this new sensor to perform three-color imaging with high spatiotemporal precision in a variety of in vitro and in vivo applications, including cultured neurons, acute brain slices, and behaving animals.

## Development and in vitro characterization of a far-red DA sensor

We used the human D1 receptor (D1R) as the scaffold because of its superior membrane trafficking properties compared with other DA receptors (10). As the first step, we replaced the third intracellular loop in D1R with an optimized circularly permuted HaloTag protein (cpHaloTag) originally derived from the Ca<sup>2+</sup> sensor HaloCaMP (23). To optimize the DA sensor, we labeled the chimera variants with far-red dyes conjugated to a HaloTag ligand, which forms a covalent bond with cpHaloTag (25). We generated the DA sensor based on the hypothesis that upon binding its ligand, the receptor undergoes a conformational change that in turn drives a conformational change in cpHaloTag, thereby shifting the equilibrium of the conjugated dye from the nonfluorescent (L) state to the fluorescent (Z) state, resulting in an increase in fluorescence (Fig. 1A). We then systematically optimized the cpHaloTag insertion sites, linker sequences, and critical residues in both cpHaloTag and D1R (fig. S1), primarily using Janelia Fluor 646 (JF646) as the far-red dye (25, 26) because of its superior bioavailability compared with JF635 (see below). We screened >2000 variants and identified the variant with the highest response, which we called HaloDA1.0 (Fig. 1B). We also generated a DA-insensitive sensor, which we called HaloDAmut, and used it as a negative control by mutating sites in the receptor's ligand-binding pocket (Fig. 1B and fig. S1A).

<sup>1</sup>Peking-Tsinghua Center for Life Sciences, New Cornerstone Science Laboratory, Academy for Advanced Interdisciplinary Studies, Peking University, Beijing, China. <sup>2</sup>PKU-IDG/McGovern Institute for Brain Research, Beijing, China. <sup>3</sup>State Key Laboratory of Membrane Biology, Peking University School of Life Sciences, Beijing, China. <sup>4</sup>Institute of Neuroscience, State Key Laboratory of Brain Cognition and Brain-Inspired Intelligence Technology, Center for Excellence in Brain Science and Intelligence Technology, Chinese Academy of Sciences, Shanghai, China. <sup>5</sup>Institute of Molecular Medicine, Peking University College of Future Technology, Beijing, China. <sup>6</sup>Department of Chemical Biology, Max Planck Institute for Medical Research, Heidelberg, Germany. <sup>7</sup>Neuroscience Institute, New York University Langone Medical Center, New York, NY, USA. <sup>8</sup>Department of Anesthesiology, Beijing Chao-Yang Hospital, Capital Medical University, Beijing, China. <sup>9</sup>Janelia Research Campus, Howard Hughes Medical Institute, Ashburn, VA, USA. <sup>10</sup>National Biomedical Imaging Center, Peking University, Beijing, China. <sup>11</sup>University of Chinese Academy of Sciences, Beijing, China. \*Corresponding author. Email: yulongli@pku.edu.cn †These authors contributed equally to this work. ‡These authors contributed equally to this work.

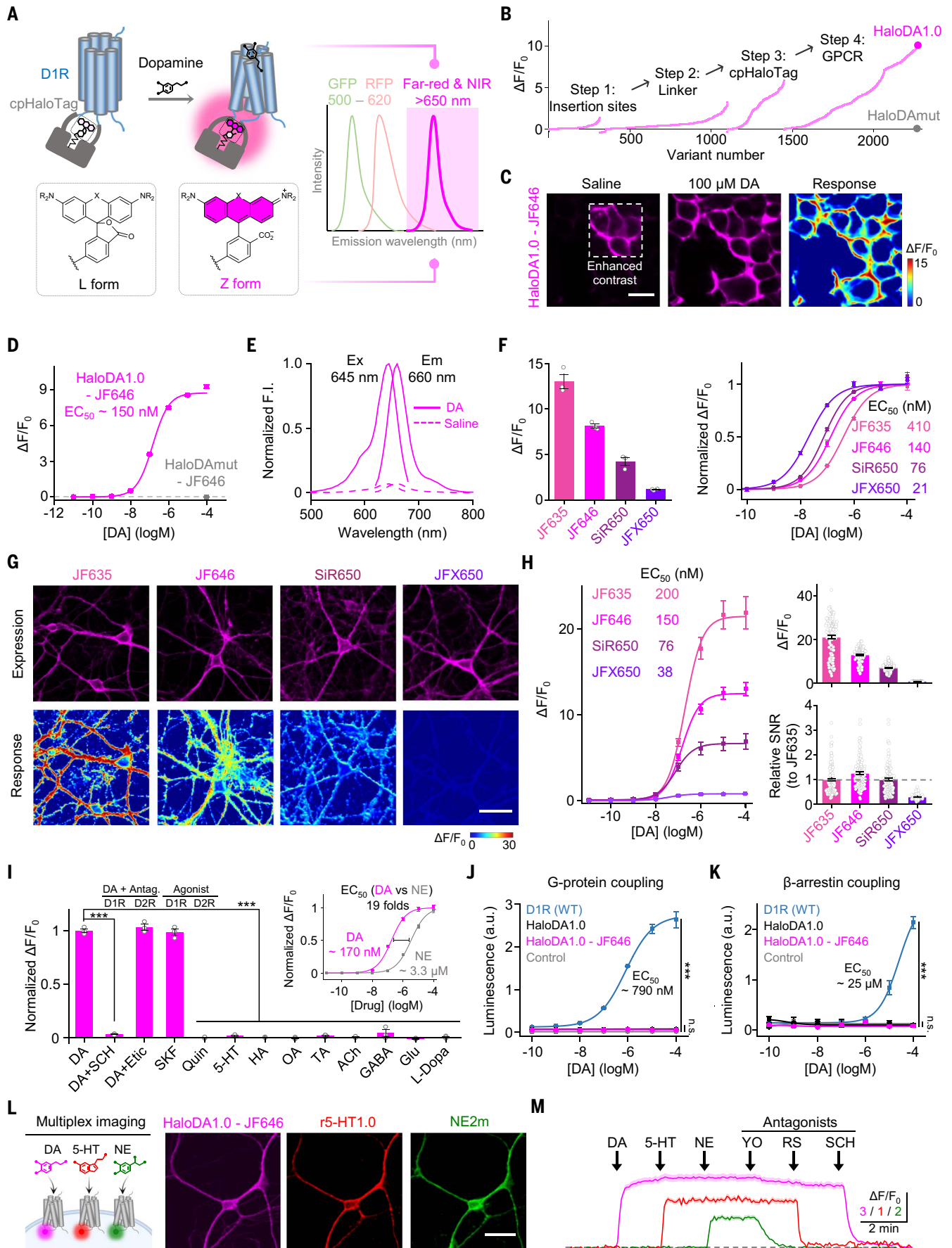


**Fig. 1. Development and characterization of a far-red dopamine sensor.** (A) Left: schematic diagram illustrating the principle of the far-red DA sensor (top) and L-Z equilibrium of rhodamine derivatives (bottom). Right: idealized traces depicting the emission spectra of current GFP- and red fluorescent protein (RFP)-based sensors alongside the new far-red and NIR sensors. (B) Optimization of far-red DA sensor variants in response to 100  $\mu\text{M}$  DA application, with stepwise changes in the insertion sites, linker, cpHaloTag, and GPCR optimization. The variants in step 1 were screened using the dye JF635, and the variants in steps 2, 3, and 4 were screened using the dye JF646. (C) Representative images of HEK293T cells expressing HaloDA1.0 and labeled with JF646 before and after application of 100  $\mu\text{M}$  DA. Scale bar, 20  $\mu\text{m}$ . (D) Dose-response curves of HaloDA1.0 and HaloDAmut labeled with JF646 in HEK293T cells.  $n = 3$  wells with 300 to 500 cells per well. (E) One-photon excitation (Ex) and emission (Em) spectra of HaloDA1.0 labeled with JF646 in the presence of 100  $\mu\text{M}$  DA (solid lines) or saline (dashed lines). F.I., fluorescence intensity. (F) Maximum  $\Delta F/F_0$  (left) and normalized dose-response curves (right) for HaloDA1.0 labeled with the indicated dyes in HEK293T cells.  $n = 3$  wells with 300 to 500 cells per well for each dye. (G) Representative images of cultured rat cortical neurons expressing HaloDA1.0 and labeled with the indicated dyes (top row) and fluorescence response to 100  $\mu\text{M}$  DA (bottom row). Scale bar, 50  $\mu\text{m}$ . (H) Dose-response curves (left), maximum  $\Delta F/F_0$  (top right), and SNR relative to JF635 (bottom right) for cultured rat cortical neurons expressing HaloDA1.0 and labeled with the indicated dyes.  $n = 120$  regions of interest (ROIs) from four coverslips for each dye. (I) Normalized  $\Delta F/F_0$  (relative to DA) for HaloDA1.0 expressed in cultured neurons and labeled with JF646. Etic, eticlopride (D2R antagonist); SKF, SKF-81297 (D1R agonist); Quin, quinpirole (D2R agonist); HA, histamine; OA, octopamine; TA, tyramine; GABA,  $\gamma$ -aminobutyric acid; Glu, glutamate; L-Dopa, levodopa. All chemicals were applied at 1  $\mu\text{M}$ .  $n = 3$  wells with an average of 50 neurons per well. The inset shows the dose-response curves for DA and NE.  $n = 3$  to 4 coverslips with 30 ROIs per coverslip. (J) Luciferase complementation assay to measure G protein coupling. Cells expressing miniGs-LgBit alone served as a negative control.  $n = 3$  wells per group. WT, wild-type. (K) Tango assay to measure  $\beta$ -arrestin coupling. Nontransfected cells served as a negative control.  $n = 3$  wells per group. (L) Schematic diagram depicting the strategy for multiplex imaging (left) and representative images (right) of cultured neurons coexpressing the far-red DA sensor JF646-labeled HaloDA1.0, the red fluorescent 5-HT sensor r5-HT1.0, and the green fluorescent NE sensor NE2m. Scale bar, 50  $\mu\text{m}$ . (M) Fluorescence responses of JF646-labeled HaloDA1.0 (magenta), r5-HT1.0 (red), and NE2m (green). Where indicated, DA (1  $\mu\text{M}$ ), 5-HT (1  $\mu\text{M}$ ), NE (1  $\mu\text{M}$ ), yohimbine (YO, 2  $\mu\text{M}$ ), RS23597-190 (RS, 20  $\mu\text{M}$ ) and SCH (10  $\mu\text{M}$ ) were applied.  $n = 40$  ROIs from three coverslips.

We first confirmed that the JF646-conjugated HaloDA1.0 sensor (HaloDA1.0-JF646) could reach the plasma membrane when expressed in human embryonic kidney (HEK) 293T cells (Fig. 1C) and produced a strong, transient increase in fluorescence upon ligand application, with a half-maximal effective concentration ( $\text{EC}_{50}$ ) of 150 nM and a maximum  $\Delta F/F_0$  of  $\sim 900\%$  (Fig. 1D). Using one-photon excitation, we then confirmed that HaloDA1.0-JF646 was in the far-red range, with an excitation peak at 645 nm and an emission peak at 660 nm (Fig. 1E). Chemical dyes, which vary in their structure and properties, can affect the performance of HaloDA1.0; therefore, we tested a wide range of rhodamine derivatives (22, 25–30) in HaloDA1.0-expressing HEK293T cells, identifying several dyes that elicited a strong response in HaloDA1.0 with spectra spanning from green to NIR (Fig. 1F and figs. S2 and S3). When labeled with distinct far-red dyes, HaloDA1.0 had peak  $\Delta F/F_0$  responses ranging from 110 to 1300% and  $\text{EC}_{50}$  values varying from 21 to 410 nM (Fig. 1F), with the fluorescence brightness and dye-labeling rate also varying substantially across dyes (fig. S4). The DA-insensitive HaloDAmut sensor, which is as bright and efficiently labeled as HaloDA1.0 (fig. S4), had no detectable fluorescence increase in response to DA application regardless of the dye used (Fig. 1D and fig. S2B). We also examined the performance of far-red dye-labeled HaloDA1.0 expressed in cultured neurons. Consistent with our results obtained with HEK293T cells, we observed a similar rank order for the four dyes tested in terms of the sensor's peak response and DA affinity (Fig. 1, G and H, and fig. S2E). These results indicate that the properties of HaloDA1.0, including its spectrum, brightness, ligand response, and ligand affinity, could be fine-tuned by labeling with specific chemical dyes.

Next, we characterized the sensor's pharmacological properties, kinetics, and coupling to downstream pathways when expressed in HEK293T cells and cultured neurons and then labeled with either JF646 or SiR650 (27) (Fig. 1, I to K, and fig. S5). We found that HaloDA1.0 retained the pharmacological properties of the parent receptor, because it could be activated by the D1R agonist SKF-81297 but not the D2R-specific agonist quinpirole. In addition, the DA-induced increase in HaloDA1.0 fluorescence was blocked by co-application of the D1R-specific antagonist SCH-23390 (hereafter SCH) but was unaffected by the D2R-specific antagonist eticlopride (Fig. 1I and fig. S5A). Moreover, HaloDA1.0 had a 15- to 19-fold higher sensitivity to DA compared with the structurally similar neuromodulator norepinephrine (NE), and had only a minimal response to a wide range of other neurochemicals tested (Fig. 1I and fig. S5, A and B). Using line-scan confocal microscopy, we locally applied DA followed by SCH to measure the sensor's on-rate ( $\tau_{\text{on}}$ ) and off-rate ( $\tau_{\text{off}}$ ), respectively. We found

that HaloDA1.0 had a subsecond on-rate (with  $\tau_{\text{on}}$  values of 40 and 90 ms when labeled with JF646 and SiR650, respectively) and an off-rate similar to values reported for DA sensors (with  $\tau_{\text{off}}$  values of 3.08 and 2.96 s when labeled with JF646 and SiR650, respectively) (fig. S5, C and D). To determine whether HaloDA1.0 coupled to downstream intracellular signaling pathways, we used the luciferase complementation assay and the Tango assay to measure Gs- and  $\beta$ -arrestin-mediated signaling, respectively. We found that HaloDA1.0 induced only minimal activation of these two signaling pathways (Fig. 1, J and K). As a positive control, we found that the wild-type D1R had robust dose-dependent coupling to both pathways (Fig. 1, J and K). As an additional verification, we investigated whether HaloDA1.0 undergoes  $\beta$ -arrestin-mediated internalization and/or desensitization when expressed in cultured neurons. We found that the DA-induced increase in HaloDA1.0 surface fluorescence was stable for at least 2 hours, indicating minimal internalization (fig. S5, E and F). These results indicate that HaloDA1.0 has high sensitivity and specificity for DA, with rapid response kinetics but without the complication of activating downstream signaling pathways.

One of the potential advantages of our far-red HaloDA1.0 sensor is that it should be compatible with multiplex imaging when combined with green and/or red fluorescent sensors. To test this, we coexpressed the far-red HaloDA1.0-JF646 sensor, the red fluorescent 5-HT sensor r5-HT1.0 (31), and the green fluorescent NE sensor NE2m (32) in cultured neurons and then performed three-color imaging using confocal microscopy. We found that all three sensors were expressed in the same neuron, and their respective fluorescence signals could be sequentially activated and blocked by application of their respective agonists and antagonists. This allowed us to simultaneously monitor all three monoamine neuromodulators in real time in cultured cells with minimal cross-talk (Fig. 1, L and M).

### The HaloDA1.0 sensor is compatible for use in multiplex imaging in acute brain slices

To assess whether HaloDA1.0 can detect endogenous DA release, we injected an adeno-associated virus (AAV)-expressing HaloDA1.0 into the nucleus accumbens (NAc) of mice. After 3 weeks (to allow for expression), we prepared acute brain slices and labeled the sensor by incubating the slices for 1 hour with JF646 (Fig. 2A). We found that applying local electrical stimuli at 20 Hz with a bipolar electrode elicited a robust, transient increase in fluorescence, with the amplitude of the response correlated with the number of stimuli (Fig. 2, B and C). The sensor's specificity for endogenous DA release was confirmed by application of the D1R antagonist SCH, which completely blocked

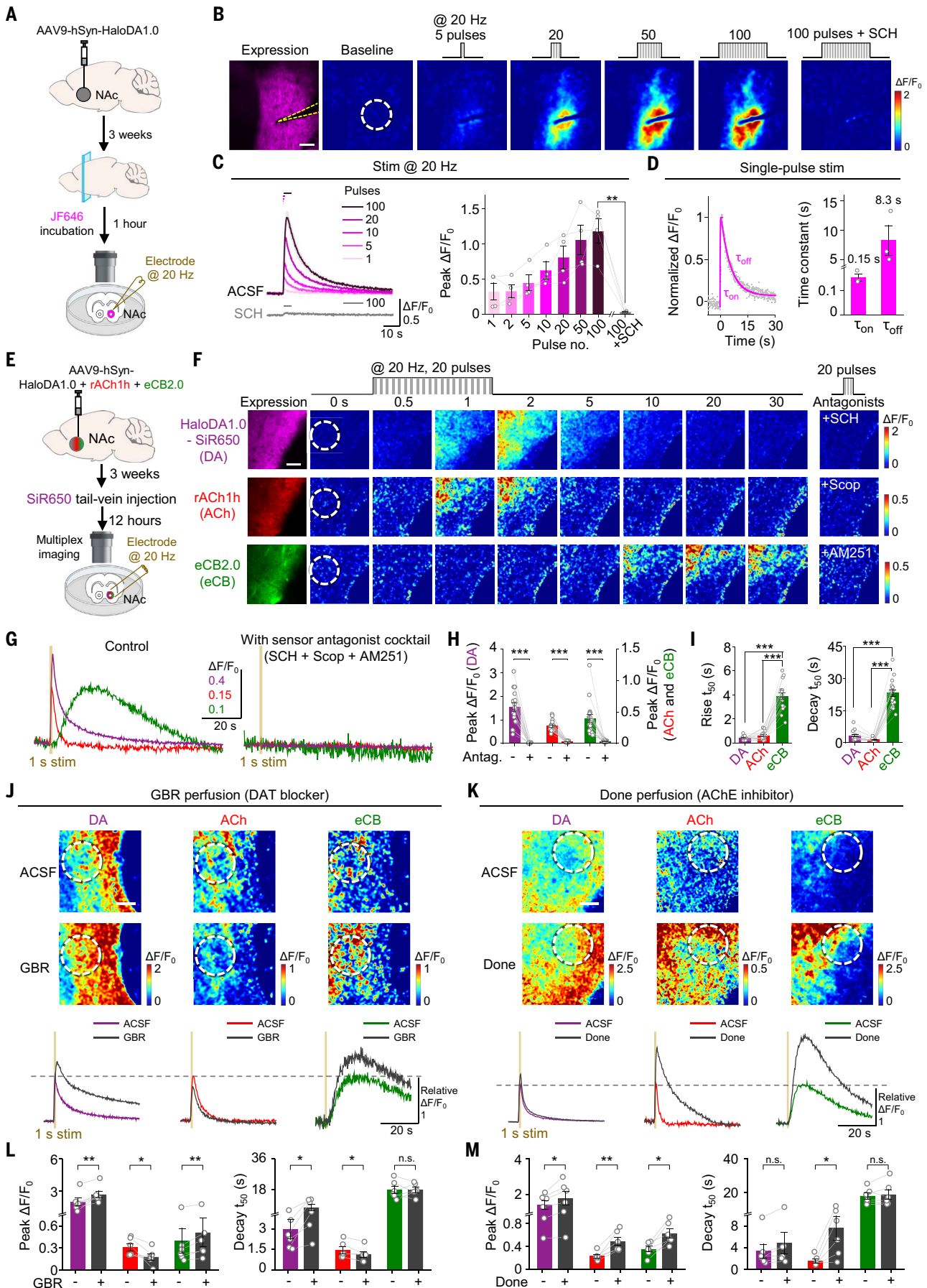


**Fig. 2. Multiplex imaging using HaloDA1.0 in acute mouse brain slices.** (A) Schematic illustration depicting the strategy for single-color imaging of mouse brain slices expressing HaloDA1.0. (B) Representative images showing the expression and fluorescence response of JF646-labeled HaloDA1.0 at baseline and in response to the indicated electrical stimuli. The white dashed circle (100  $\mu\text{m}$  diameter) indicates the ROI used for further analysis, and the approximate location of the stimulating electrode is indicated with dashed yellow lines. SCH concentration was 10  $\mu\text{M}$ . Scale bar, 50  $\mu\text{m}$ . (C) Representative traces (left) and group summary (right) of the changes in JF646-labeled HaloDA1.0 fluorescence in response to the indicated number of electrical stimuli.  $n = 4$  slices from 3 mice. (D) Representative trace showing normalized  $\Delta F/F_0$  (left) and group summary of  $\tau_{\text{on}}$  and  $\tau_{\text{off}}$  (right) measured in response to a single electrical stimulus. The trace was fitted with single-exponential functions to determine  $\tau_{\text{on}}$  and  $\tau_{\text{off}}$ .  $n = 3$  slices from 3 mice. (E) Schematic illustration depicting the strategy for multiplex imaging of mouse brain slices prepared 12 hours after injecting 100 nmol SiR650 into the mouse's tail vein. (F) Representative images showing the expression and time-lapse fluorescence responses of SiR650-labeled HaloDA1.0, rACh1h, and eCB2.0 in response to the indicated electrical stimuli. The fluorescence response of each sensor measured in the presence of its corresponding antagonist [SCH, scopolamine (Scop), or AM251, applied at 10  $\mu\text{M}$ ] is shown on the far right. The white dashed circle (100  $\mu\text{m}$  diameter) indicates the ROI used for further analysis. Scale bar, 50  $\mu\text{m}$ . (G and H) Representative traces (G) and group summary (H) of the fluorescence change in SiR650-labeled HaloDA1.0 (magenta), rACh1h (red), and eCB2.0 (green) in response to electrical stimuli (20 Hz applied for 1 s) before and after application of the antagonist cocktail.  $n = 18$  slices from 6 mice. (I) Group summary of the rise and decay kinetics ( $t_{50}$ ) of all three sensors in response to electrical stimuli. (J and K) Representative pseudocolor images (top) and traces of the fluorescence response [bottom, relative to artificial cerebrospinal fluid (ACSF)] of the indicated sensors in response to electrical stimuli (20 Hz applied for 1 s) before and after the application of 2  $\mu\text{M}$  GBR (J) or donepezil (Done) (K). Scale bar, 50  $\mu\text{m}$ . (L and M) Group summary of peak  $\Delta F/F_0$  (left) and decay  $t_{50}$  (right) for the indicated three sensors in response to electrical stimuli in the presence of GBR (L) or donepezil (M).  $n = 6$  slices from 3 mice for each treatment.

the fluorescence increase (Fig. 2, B and C). HaloDA1.0 showed high sensitivity, because it was able to detect DA release induced by a single electrical pulse with a mean rise time constant of 150 ms and a mean decay time constant of 8.3 s (Fig. 2D).

In addition to DA, a variety of other neuromodulators, such as ACh and eCBs, are also released in the NAc, and although their interaction with DA has physiological relevance, this cross-talk between neuromodulator systems remains poorly understood (6, 33). This intricate network of neuromodulators in the NAc therefore provides an excellent model system for performing multiplex imaging in a physiological context. We injected a mixture of viruses expressing HaloDA1.0 (subsequently labeled with the far-red dye SiR650 by tail vein injection), rACh1h (for ACh) (34), and the green fluorescent eCB sensor eCB2.0 (35) in the NAc. This allowed us to monitor all three neuromodulators simultaneously using confocal microscopy in acute mouse brain slices (Fig. 2E). We found that all three sensors had a robust increase in their respective fluorescence signals in response to field stimuli applied at 20 Hz; moreover, each sensor's signal was blocked by application of its respective antagonist, confirming specificity (Fig. 2, F to H). Compared with the DA and ACh signals, the eCB signal had slower rise and decay times, with an onset of eCB release occurring after the end of the stimulus (Fig. 2I), consistent with previous electrophysiological studies (36–38). Although sensor kinetics may partially affect the signal kinetics, the predominant factor is likely their different release mechanism, because eCB needs time to be synthesized for release (39, 40), whereas DA and ACh are directly released from the vesicles upon stimulus (41, 42).

Our successful use of three-color imaging to measure three distinct neuromodulators provides a good system in which to study their regulation. We therefore pretreated brain slices with the selective DA transporter (DAT) blocker GBR12909 (hereafter GBR) and found that it both increased the peak response and slowed the decay kinetics of the stimulus-induced DA signal (Fig. 2, J and L), consistent with reduced reuptake of DA into the presynaptic terminal. Moreover, GBR reduced the peak ACh signal (Fig. 2, J and L), consistent with the notion that DA inhibits ACh release by binding D2R on cholinergic interneurons (43–45). GBR also increased the peak eCB signal (Fig. 2, J and L). Similarly, the acetylcholinesterase inhibitor donepezil increased the stimulus-induced ACh signal and also modestly increased the DA signal (Fig. 2, K and M), consistent with ACh's known mechanism of action through nicotinic ACh receptors at dopaminergic terminals (46–48). Donepezil also increased the peak eCB signal (Fig. 2, K and M), suggesting a previously unknown interaction between the ACh and eCB signaling pathways. These results demonstrate that HaloDA1.0 is suitable for use in multiplex imaging and provide new insights into the cross-talk among three key neuromodulators.

### Multiplex imaging in zebrafish larvae

To determine whether HaloDA1.0 can be used to monitor DA dynamics in vivo, we transiently expressed the sensor in neurons in larval zebrafish, leveraging their genetic accessibility and optical transparency. We then labeled the sensor using three far-red dyes, JF635, JF646, and SiR650, and found that SiR650-labeled sensors had the strongest baseline fluorescence (fig. S6, A and C). Both JF646 and SiR650 displayed relatively low background staining,  $\sim 1\%$  of sensor fluorescence (fig. S6D). Moreover, locally applying a puff of DA rapidly induced a robust, transient increase in fluorescence, with the largest response measured in JF646-labeled sensors (fig. S6, B and E). SiR650- and JF646-labeled sensors had a similar signal-to-noise ratio (SNR), outperforming JF635-labeled sensors (fig. S6F). As negative controls, we confirmed that a puff of phosphate-buffered saline had no effect on SiR650-labeled HaloDA1.0, and DA had no effect on SiR650-labeled HaloDAmut (fig. S6, B, E, and F).

We then performed three-color in vivo imaging in zebrafish larvae by transiently expressing HaloDA1.0 in a zebrafish line expressing the red fluorescent  $\text{Ca}^{2+}$  sensor jRGECO1a in neurons and the green fluorescent ATP sensor ATP1.0 (49) in astrocytes (fig. S7A). The HaloDA1.0 sensor was then labeled with SiR650. Upon application of a mild electrical body shock, we observed time-locked fluorescence increases for all three sensors in the hindbrain (fig. S7, B and D). The kinetics of the DA and ATP signals were similar, but both signals decayed more slowly than the neuronal  $\text{Ca}^{2+}$  signal (fig. S7F). In addition, we found strong correlation between the DA and ATP signals, with a negligible time lag between the two (fig. S7F). In addition, application of the GABA<sub>A</sub> receptor antagonist pentylenetetrazole (PTZ) induced robust, synchronized DA and ATP signals that were in phase with the neuronal  $\text{Ca}^{2+}$  signal (fig. S7, C and E). By aligning the DA and ATP signals with the peak  $\text{Ca}^{2+}$  signal, we found a high correlation in peak amplitude between the DA and  $\text{Ca}^{2+}$  signals and between the ATP and  $\text{Ca}^{2+}$  signals (fig. S7G). Furthermore, we found that the decay kinetics of the DA signals differed between signals induced by electrical shock and those induced by PTZ application. By contrast, we found no difference in decay kinetics for the  $\text{Ca}^{2+}$  and ATP signals (fig. S7H). These results indicate that the HaloDA1.0 sensor can reliably detect DA release in vivo and is compatible for use in three-color imaging in the brain of zebrafish larvae.

### HaloDA1.0 can detect optogenetically evoked DA release in freely moving mice

Using a cpHaloTag-based sensor in vivo in mice requires delivery of the dye to the mouse's brain, presenting a greater challenge compared with its use in zebrafish. Therefore, we systematically compared various far-red dyes in vivo to optimize the performance of HaloDA1.0. We virally expressed the optogenetic actuator Channelrhodopsin-2 (ChR2) in the ventral tegmental area (VTA) and expressed HaloDA1.0 in the NAc (Fig. 3A and fig. S8A), which receives dense dopaminergic

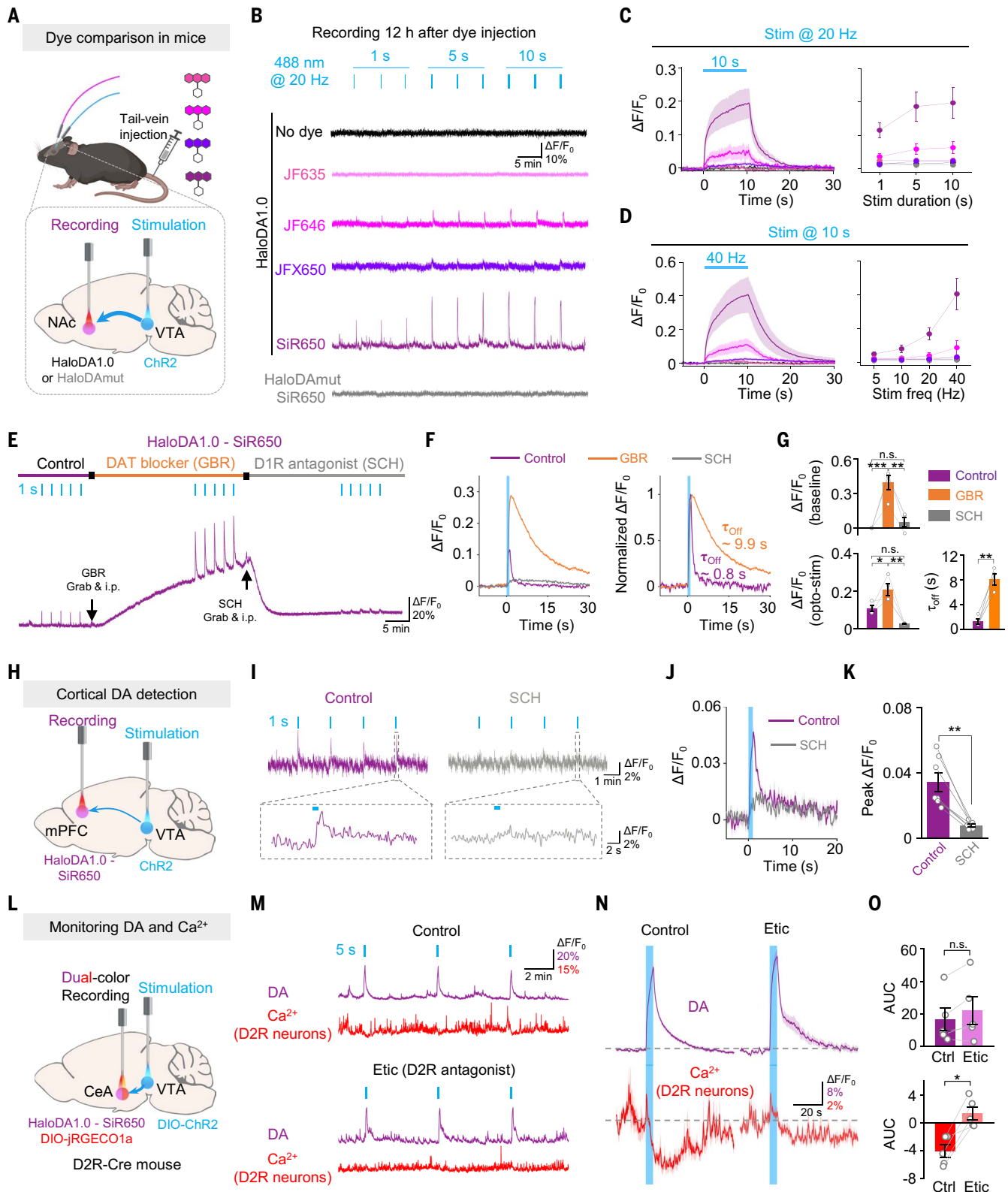


**Fig. 3. HaloDA1.0 can be used to detect endogenous DA release in freely moving mice.** (A) Schematic diagram depicting the strategy for using fiber photometry to record HaloDA1.0 or HaloDAmut labeled with various dyes (100 nmol injected through the tail vein) in the NAC upon optogenetic stimulation of VTA neurons. (B) Representative traces of the change in HaloDA1.0 or HaloDAmut fluorescence during optogenetic stimulation in the indicated mice. (C and D) Average traces (left) and group summary (right) of the change in HaloDA1.0 or HaloDAmut fluorescence measured under the indicated stimulation duration (C) and frequency (D).  $n = 3$  to 5 mice per group. (E) Representative trace of the change in HaloDA1.0 fluorescence measured at baseline (control), after an intraperitoneal injection of 20 mg/kg GBR, and after an intraperitoneal injection of 8 mg/kg SCH. The blue ticks indicate the optogenetic stimuli. (F) Averaged trace (left) and normalized traces (right) of SiR650-labeled HaloDA1.0 measured in one mouse under the indicated conditions. The vertical blue shading indicates the optogenetic stimuli, and the off kinetics ( $\tau_{off}$ ) were fitted with a single-exponential

function. **(G)** Group summary of baseline  $\Delta F/F_0$  (top), peak  $\Delta F/F_0$  (bottom left), and  $\tau_{\text{off}}$  (bottom right) measured for SiR650-labeled HaloDA1.0 under the indicated conditions.  $n = 4$  mice. **(H)** Schematic illustration depicting the strategy for fiber photometry recording of HaloDA1.0 in the mPFC upon optogenetic stimulation of VTA neurons. **(I)** Representative traces and magnified view (indicated by dashed box) of the change in fluorescence of SiR650-labeled HaloDA1.0 under the indicated conditions. The blue ticks indicate the optogenetic stimuli applied at 20 Hz for 1 s. **(J and K)** Average traces (J) and group summary (K) of peak  $\Delta F/F_0$  for SiR650-labeled HaloDA1.0 under the indicated conditions.  $n = 7$  mice. **(L)** Schematic diagram depicting the strategy for dual-color fiber photometry recording in the CeA with optogenetic stimulation of VTA neurons in a D2R-Cre mouse. **(M and N)** Representative traces (M) and average traces (N) of the DA and  $\text{Ca}^{2+}$  signals measured in D2R-expressing neurons in the same mouse under control conditions or after application of 2 mg/kg Etic. The blue ticks and vertical shading indicate the optogenetic stimuli applied at 20 Hz for 5 s. The traces in (N) represent the average of eight trials per condition. **(O)** Group summary of the area under the curve (AUC, 0 to 30 s) of the DA and  $\text{Ca}^{2+}$  signals measured under the indicated conditions.  $n = 5$  mice per group.

projections from the VTA. We then injected various dyes into the tail vein to label HaloDA1.0 in the NAc and performed fiber photometry recordings 12 hours later, by which time the background staining was minimal (50, 51). Optogenetic stimulation of the VTA resulted in a moderate increase in JF646-labeled HaloDA1.0 fluorescence, with no measurable change in JF635-labeled or JFX650-labeled HaloDA1.0 (Fig. 3, B to D). By contrast, and consistent with our results obtained with zebrafish, SiR650-labeled HaloDA1.0 had a much higher response. To elucidate the performance discrepancy of different far-red dyes in vitro and in vivo, we quantified their labeling efficiency in mice using a pulse-chase assay (51, 52). The results showed a higher labeling percentage for SiR650 compared with the other far-red dyes (fig. S9), supporting the superior performance of SiR650 observed in the in vivo recordings. SiR650-labeled HaloDA1.0 provided higher brightness than fluorescent proteins in vivo, in both zebrafish and mice (fig. S10). As negative controls, no signal was detected in uninjected mice or in mice expressing SiR650-labeled HaloDAmut (Fig. 3, B to D). In addition, an intraperitoneal injection of the DAT blocker GBR produced a slow progressive increase in the basal fluorescence of SiR650-labeled HaloDA1.0 and increased both the magnitude and decay time of the light-activated responses (Fig. 3, E to G). Moreover, the D1R antagonist SCH application abolished both the increase in basal fluorescence and the light-evoked responses. The optogenetically evoked signals were stable for 2 days but then decreased, presumably due to degradation of the sensor-dye complex because the responses were restored by subsequent injections of dye (fig. S11). These results indicate that expressing HaloDA1.0 and then labeling the sensor with SiR650 provides a sensitive and specific tool for monitoring the release of endogenous DA in vivo in mice.

Next, we investigated whether HaloDA1.0 can be used to monitor DA release in vivo in sparsely innervated brain regions such as the medial prefrontal cortex (mPFC) (53, 54). We found that activation of neurons in the VTA caused transient increases in SiR650-labeled HaloDA1.0 in the mPFC, and these responses were blocked by SCH (Fig. 3, H to K, and fig. S8B). We compared the performance of HaloDA1.0 with reported DA sensors and found that HaloDA1.0 exhibited larger fluorescence increases than gDA3m (13) and dLight1.3b (15), demonstrating its high sensitivity to detect modest DA release in vivo in mice (fig. S12).

To test whether our far-red sensor is compatible for use in dual-color recordings during optogenetic stimulation, we expressed DIO-ChR2 in the VTA of D2R-Cre mice to specifically activate dopaminergic neurons, because D2R can serve as a general marker for these neurons in the VTA (55, 56). In addition, we co-expressed HaloDA1.0 and the red fluorescent  $\text{Ca}^{2+}$  sensor DIO-jRGECO1a in the central nucleus of the amygdala (CeA), which abundantly expresses DA receptors and receives dopaminergic projections from the VTA (53, 57, 58), to determine how DA release affects neuronal activity in the CeA (Fig. 3L and fig. S8C). We found that optogenetic stimuli triggered an increase in DA release together with a decrease in  $\text{Ca}^{2+}$  in D2R-positive neurons (Fig. 3, M to O). Moreover, treatment with the D2R antagonist eticlopride blocked the change in  $\text{Ca}^{2+}$  without affecting DA release (Fig. 3, M to O), indicating that DA may suppress the activity of D2R-positive neurons in the CeA by activating inhibitory D2R signaling.

## Simultaneously monitoring DA, ACh, and cAMP dynamics in the mouse NAc

In the striatum, both DA and ACh play essential roles in learning and motivation, regulating synaptic plasticity in part by binding to the excitatory D1R and the inhibitory muscarinic acetylcholine M4 receptor (M4R), respectively, expressed on medium spiny neurons (D1-MSNs) (59–63). Although several pioneering studies examined the interaction between DA and ACh signaling (46, 64, 65), the effects of their concurrent regulation on intracellular cAMP signaling in D1-MSNs during behavior remain poorly understood. To address this important issue, we virally coexpressed HaloDA1.0, rACh1h, and the green fluorescent cAMP sensor DIO-GFlamp2 (66, 67) in the NAc of D1R-Cre mice (Fig. 4, A and B). We then labeled the DA sensor with SiR650 and used three-color fiber photometry to simultaneously monitor DA, ACh, and cAMP in vivo (Fig. 4 and fig. S13).

All three signals showed spontaneous fluctuations in the absence of stimuli (Fig. 4C). Centering on the peaks of the spontaneous DA fluctuations, we observed a corresponding increase in the cAMP signal and a phasic dip in the ACh signal (Fig. 4, E and I). The peak in DA preceded the trough in the ACh signal, followed by the peak in cAMP, which is consistent with the requirement for DA to bind D1R to produce cAMP. During unconditioned sucrose rewards, we observed a pattern akin to the spontaneous signals (Fig. 4, C, F, and J); however, upon applying a 1-s foot shock, a distinct pattern emerged for all three signals (Fig. 4, G and K). We then ruled out spectral crosstalk between the three sensors and confirmed the specificity of the signals by showing that SCH largely eliminated the DA and cAMP signals, whereas the M3R antagonist Scop selectively blocked the ACh signal (fig. S14). Given the comparable sensor kinetics (34, 66), the rise and decay differences in these signals are majorly due to the changes in the amounts of DA, ACh, and cAMP. Finally, a correlation analysis revealed a direct correlation between DA and cAMP (with a 500-ms lag) and inverse correlations both between ACh and cAMP and between DA and ACh (both with a 300-ms lag) (Fig. 4M), consistent with recent studies regarding the interaction between DA and ACh (64, 65).

Combining their dynamics and receptor functions, we found that both the increase in DA and the decrease in ACh signals facilitate the production of cAMP during spontaneous activity and in response to sucrose (fig. S15). Conversely, both the decrease in DA and the increase in ACh signals in response to aversive stimuli (in this case, foot shock) reduce cAMP production. We therefore investigated the effect of the addictive drug cocaine on this regulatory mechanism. We found that a single intraperitoneal injection of 20 mg/kg cocaine increased all three signals, with the DA and cAMP signals being substantially larger than the signals induced by sucrose (Fig. 4, H and L, and fig. S13). In addition, we found a strong direct correlation between all three pairs of signals (Fig. 4N), suggesting that cocaine can disrupt the normal interactions between these signaling processes (fig. S15). Together, these in vivo experiments provide a comprehensive view of the dynamic interplay between DA, ACh, and cAMP in D1-MSNs under different conditions, highlighting the ability of using HaloDA1.0 to measure the subsecond dynamics and interplay between these neurochemicals in vivo in mice.

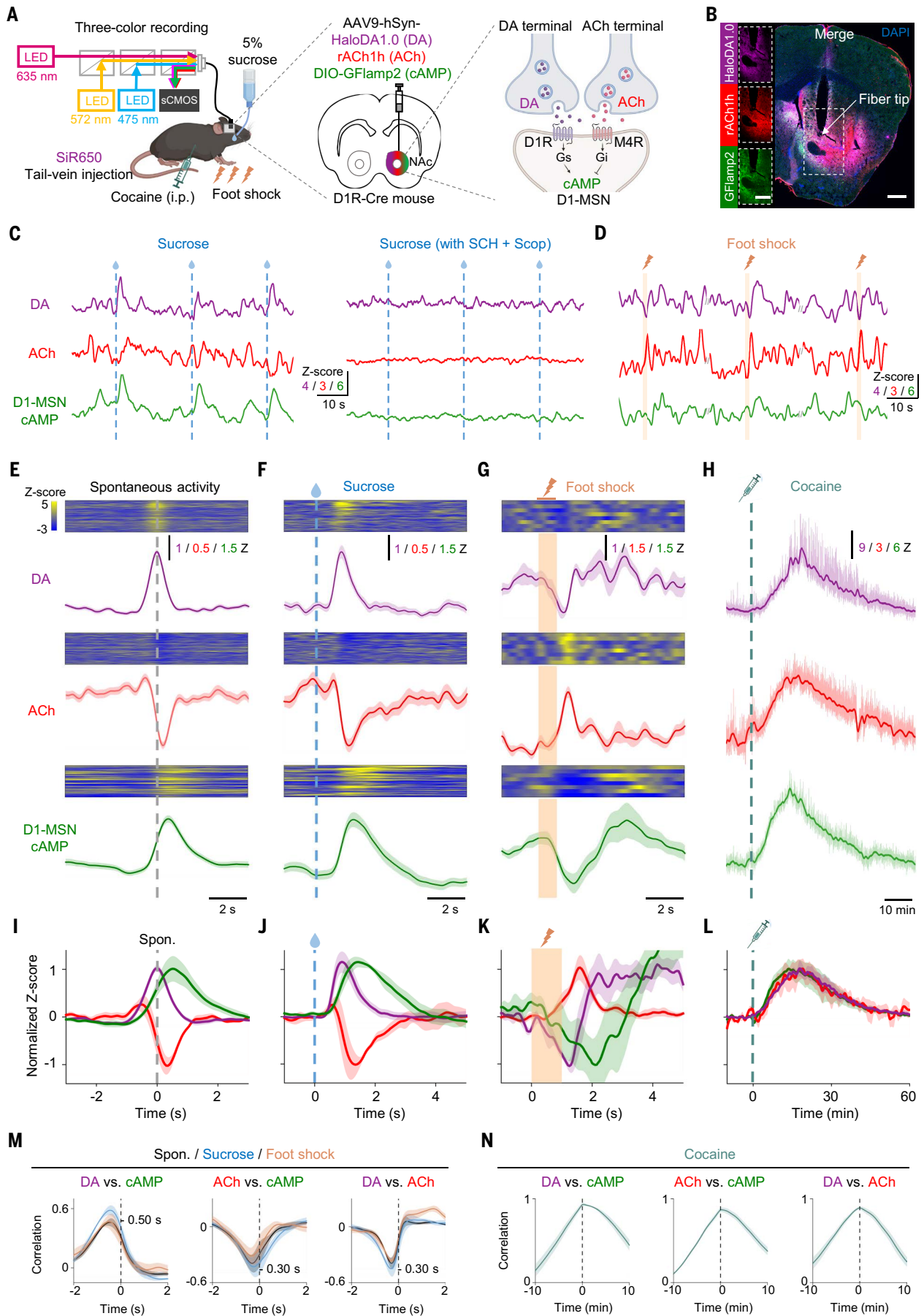


**Fig. 4. Simultaneous monitoring of DA, ACh, and cAMP dynamics in vivo in mice.** (A) Left and middle: schematic diagram depicting the strategy for three-color fiber photometry recording of DA, ACh, and D1-MSN cAMP signals in the NAc during 5% sucrose delivery, foot shock (0.7 mA for 1 s), or after an intraperitoneal injection of cocaine (20 mg/kg). Right: proposed model for the actions of DA and ACh in D1-MSNs. DA released from the dopaminergic termini binds Gs-coupled D1R to drive cAMP production. ACh released from cholinergic interneurons binds Gi-coupled M4R to reduce cAMP production. (B) Histological verification of HaloDA1.0, rACh1h, and DIO-GFlamp2 expression in the mouse NAc. The white arrow indicates the approximate location of the fiber tip. Images of the individual channels are shown on the left. Scale bars, 0.5 mm. (C) Example traces of all three sensor signals measured simultaneously in the NAc during three consecutive sucrose trials under control conditions (left) or after intraperitoneal injection of 8 mg/kg SCH and 10 mg/kg Scop (right). (D) Example traces of all three sensor signals measured simultaneously in the NAc during three consecutive foot shock trials. (E to H) Representative time-aligned pseudocolor images and average traces of DA, ACh, and D1-MSN cAMP signals measured in a mouse during spontaneous activity (E), sucrose (F), foot shock (G), and cocaine application (H). The traces in (E), (F), and (G) are shown as the mean  $\pm$  SEM. In (H), the raw fluorescent response is indicated by the shaded area, and the bold lines indicate the response after low-pass filtering at 0.01 Hz. (I to L) Normalized fluorescence response of all three sensor signals measured during spontaneous activity (I), sucrose (J), foot shock (K), and cocaine application (L).  $n = 4$  mice each. (M and N) Mean cross-correlation between the indicated pairs of sensor signals measured under the indicated conditions. The cross-correlations during spontaneous activity, sucrose, and foot shock application are shown in (M), with the time lag indicated. The cross-correlations during cocaine application are shown in (N).  $n = 4$  mice for each condition.

## Discussion

Here, we report the development, characterization, and application of HaloDA1.0, a far-red chemigenetic DA sensor with distinct spectral properties that make it compatible for use with existing sensors for monitoring other neuromodulators. By combining HaloDA1.0 with existing green and red fluorescent neuromodulator sensors,  $\text{Ca}^{2+}$  indicators, cAMP sensors, and optogenetic tools, we show that this DA sensor can be used for multicolor imaging in a variety of models. In cultured neurons, we simultaneously imaged the dynamics of three monoamines. In acute mouse brain slices, we imaged the release of—and then studied the regulation of—endogenous DA, ACh, and eCB upon electrical stimulation. Using zebrafish larvae, we imaged endogenous DA, ATP, and  $\text{Ca}^{2+}$  signals. We also showed that this sensor can detect DA release in vivo in mice, using dual-color recording to measure changes in DA and intracellular  $\text{Ca}^{2+}$  in response to blue light-activated optogenetics. Finally, we simultaneously measured DA, ACh, and cAMP in vivo in the NAc of behaving mice under basal conditions and during various behavioral stimuli, including sucrose, foot shock, and cocaine administration, revealing distinct patterns regulating these three signaling molecules.

Unlike genetically encoded DA sensors, HaloDA1.0 uses the chemical dye cpHaloTag as its fluorescent module, in which the DA-dependent change in fluorescence relies on a shift in the equilibrium between dye's L and Z forms. Despite using a different mechanism compared with conventional genetically encoded DA sensors, HaloDA1.0 showed excellent sensitivity, good membrane trafficking, high specificity for DA, rapid kinetics, and minimal downstream coupling (68). HaloDA1.0 might also be used to monitor DA release in a wide range of brain regions, including the CeA and mPFC, making it a valuable additional tool. It is important to note that the repeated dye injection that is necessary for longitudinal recording over weeks may introduce variability in the recorded signals. Therefore, longitudinal studies using this sensor must be carefully conducted with appropriate controls and thorough validation to ensure data reliability.

When labeled with different dyes, HaloDA1.0 exhibited varying  $\text{EC}_{50}$  values, possibly caused by allosteric modulation of the GPCR. For example, classic studies suggest that G protein interactions with the intracellular domain of the GPCR stabilize the receptor in a high-affinity state (69, 70). Additionally, small molecules can act as allosteric modulators, regulating the binding affinity of GPCRs (71). Therefore, we speculate that the differences in  $\text{EC}_{50}$  across different dye labels may arise from a similar allosteric modulation mechanism of the GPCR. A similar trend has been observed in other chemigenetic sensors such as HaloCaMP1a (23).

Although the cpHaloTag-based chemigenetic strategy, which modulates L-Z equilibrium, has been used to develop both  $\text{Ca}^{2+}$  and voltage sensors (23, 24), the in vivo applications remain scarce. Identifying an appropriate dye for use in vivo is essential but challenging, requiring the right balance between its tunable properties and bioavailability. Although some JF dyes, such as JF525 and JF669, demonstrate good blood-brain barrier (BBB) permeability (22, 72, 73), they could not be used for labeling the HaloDA1.0 sensor. Here, we found that the dye

SiR650 provided the best performance in vivo, presumably due to its high bioavailability. SiR650 achieved a labeling efficiency of  $\sim 11\%$  for HaloDA1.0 in mice, leaving substantial room for improvement. Future modifications to the dye's structure and protein engineering are likely to further improve the dye-labeling rate, achieving even better performance in vivo. Additionally, a tryptophan quenching-based  $\text{Ca}^{2+}$  sensor has been recently reported (74), which bypasses the regulation of the L-Z equilibrium and is compatible with JF dyes that exhibit satisfying BBB penetration. This sensor has been well demonstrated in vivo in mice, zebrafish, and flies and could also be expanded for engineering neuromodulator sensors.

The ability to simultaneously measure DA, ACh, and cAMP in D1-MSNs within the NAc during various behaviors provides a highly comprehensive view of how neuromodulators and their downstream signals can integrate to modulate synaptic plasticity. Compared with previous studies that focused primarily on either the interaction between DA and ACh (46, 64, 65) or the interaction between DA and its downstream signals (8, 75), our three-color recording system is more robust, yielding deeper insights than single-color and even dual-color recordings. Our findings suggest a potential synergistic modulation of D1-MSNs by DA and ACh under physiological conditions, and this delicate balance can be disrupted—for example, by cocaine. This is consistent with previous studies showing that knocking out M4R in D1-MSNs potentiates cocaine-induced hyperlocomotor activity (76).

Leveraging this chemigenetic strategy, we speculate that in the future it will be possible to develop a wide range of far-red neuromodulator sensors based on other GPCRs. Given the  $>100$  neurotransmitters and neuromodulators identified to date, this strategy will offer more options for researchers to simultaneously monitor multiple neurochemical signals. Moreover, by leveraging NIR dyes and protein-engineering strategies (21, 22, 77), the sensors' spectral range can be shifted even further into the NIR range, making them even more suitable for use in in vivo imaging. Ultimately, additional protein tags such as SNAP-tag (78) and TMP-tag (79) might be used to develop sensors that are orthogonal to existing cpHaloTag sensors, providing the ability to simultaneously image a multitude of neuromodulators.

In summary, our far-red chemigenetic DA sensor, which is suitable for both in vitro and in vivo applications, can be used to simultaneously measure multiple neurochemical signals in real time. This robust tool can therefore be used to increase our understanding of the regulatory mechanisms and specific roles of the dopaminergic system under both physiological and pathological conditions.

Materials and methods are available in the supplementary materials.

## REFERENCES AND NOTES

1. L. Luo, Architectures of neuronal circuits. *Science* **373**, eabg7285 (2021). doi: [10.1126/science.abg7285](https://doi.org/10.1126/science.abg7285); pmid: [34516844](https://pubmed.ncbi.nlm.nih.gov/34516844/)
2. T. Sippy, N. X. Tritsch, Unraveling the dynamics of dopamine release and its actions on target cells. *Trends Neurosci.* **46**, 228–239 (2023). doi: [10.1016/j.tins.2022.12.005](https://doi.org/10.1016/j.tins.2022.12.005); pmid: [36635111](https://pubmed.ncbi.nlm.nih.gov/36635111/)

3. A. M. Graybiel, T. Aosaki, A. W. Flaherty, M. Kimura, The basal ganglia and adaptive motor control. *Science* **265**, 1826–1831 (1994). doi: [10.1126/science.8091209](https://doi.org/10.1126/science.8091209); pmid: [8091209](https://pubmed.ncbi.nlm.nih.gov/8091209/)
4. R. A. Wise, Dopamine, learning and motivation. *Nat. Rev. Neurosci.* **5**, 483–494 (2004). doi: [10.1038/nrn1406](https://doi.org/10.1038/nrn1406); pmid: [15152198](https://pubmed.ncbi.nlm.nih.gov/15152198/)
5. W. Schultz, P. Dayan, P. R. Montague, A neural substrate of prediction and reward. *Science* **275**, 1593–1599 (1997). doi: [10.1126/science.275.5306.1593](https://doi.org/10.1126/science.275.5306.1593); pmid: [9054347](https://pubmed.ncbi.nlm.nih.gov/9054347/)
6. D. M. Lovinger *et al.*, Local modulation by presynaptic receptors controls neuronal communication and behaviour. *Nat. Rev. Neurosci.* **23**, 191–203 (2022). doi: [10.1038/s41583-022-00561-0](https://doi.org/10.1038/s41583-022-00561-0); pmid: [35228740](https://pubmed.ncbi.nlm.nih.gov/35228740/)
7. K. Z. Peters, J. F. Cheer, R. Tonini, Modulating the neuromodulators: Dopamine, serotonin, and the endocannabinoid system. *Trends Neurosci.* **44**, 464–477 (2021). doi: [10.1016/j.tins.2021.02.001](https://doi.org/10.1016/j.tins.2021.02.001); pmid: [33674134](https://pubmed.ncbi.nlm.nih.gov/33674134/)
8. S. J. Lee *et al.*, Cell-type-specific asynchronous modulation of PKA by dopamine in learning. *Nature* **590**, 451–456 (2021). doi: [10.1038/s41586-020-03050-5](https://doi.org/10.1038/s41586-020-03050-5); pmid: [33361810](https://pubmed.ncbi.nlm.nih.gov/33361810/)
9. P. Greengard, P. B. Allen, A. C. Nairn, Beyond the dopamine receptor: The DARPP-32/protein phosphatase-1 cascade. *Neuron* **23**, 435–447 (1999). doi: [10.1016/S0896-6273\(00\)80798-9](https://doi.org/10.1016/S0896-6273(00)80798-9); pmid: [10433257](https://pubmed.ncbi.nlm.nih.gov/10433257/)
10. Y. Zhuo *et al.*, Improved green and red GRAB sensors for monitoring dopaminergic activity in vivo. *Nat. Methods* **21**, 680–691 (2024). doi: [10.1038/s41592-023-02100-w](https://doi.org/10.1038/s41592-023-02100-w); pmid: [38036855](https://pubmed.ncbi.nlm.nih.gov/38036855/)
11. F. Sun *et al.*, A genetically encoded fluorescent sensor enables rapid and specific detection of dopamine in flies, fish, and mice. *Cell* **174**, 481–496.e19 (2018). doi: [10.1016/j.cell.2018.06.042](https://doi.org/10.1016/j.cell.2018.06.042); pmid: [30007419](https://pubmed.ncbi.nlm.nih.gov/30007419/)
12. T. Patriarichi *et al.*, Ultrafast neuronal imaging of dopamine dynamics with designed genetically encoded sensors. *Science* **360**, eaat4422 (2018). doi: [10.1126/science.aat4422](https://doi.org/10.1126/science.aat4422); pmid: [29853555](https://pubmed.ncbi.nlm.nih.gov/29853555/)
13. T. Patriarichi *et al.*, An expanded palette of dopamine sensors for multiplex imaging in vivo. *Nat. Methods* **17**, 1147–1155 (2020). doi: [10.1038/s41592-020-0936-3](https://doi.org/10.1038/s41592-020-0936-3); pmid: [32895537](https://pubmed.ncbi.nlm.nih.gov/32895537/)
14. F. Sun *et al.*, Next-generation GRAB sensors for monitoring dopaminergic activity in vivo. *Nat. Methods* **17**, 1156–1166 (2020). doi: [10.1038/s41592-020-00981-9](https://doi.org/10.1038/s41592-020-00981-9); pmid: [33087905](https://pubmed.ncbi.nlm.nih.gov/33087905/)
15. Z. Wu, D. Lin, Y. Li, Pushing the frontiers: Tools for monitoring neurotransmitters and neuromodulators. *Nat. Rev. Neurosci.* **23**, 257–274 (2022). doi: [10.1038/s41583-022-00577-6](https://doi.org/10.1038/s41583-022-00577-6); pmid: [35361961](https://pubmed.ncbi.nlm.nih.gov/35361961/)
16. D. M. Shcherbakova, Near-infrared and far-red genetically encoded indicators of neuronal activity. *J. Neurosci. Methods* **362**, 109314 (2021). doi: [10.1016/j.jneumeth.2021.109314](https://doi.org/10.1016/j.jneumeth.2021.109314); pmid: [34375713](https://pubmed.ncbi.nlm.nih.gov/34375713/)
17. D. M. Shcherbakova, O. V. Stepanenko, K. K. Turoverov, V. V. Verkhusha, Near-infrared fluorescent proteins: Multiplexing and optogenetics across scales. *Trends Biotechnol.* **36**, 1230–1243 (2018). doi: [10.1016/j.tibtech.2018.06.011](https://doi.org/10.1016/j.tibtech.2018.06.011); pmid: [30041828](https://pubmed.ncbi.nlm.nih.gov/30041828/)
18. G. V. Los *et al.*, HaloTag: A novel protein labeling technology for cell imaging and protein analysis. *ACS Chem. Biol.* **3**, 373–382 (2008). doi: [10.1021/cb800025k](https://doi.org/10.1021/cb800025k); pmid: [18533659](https://pubmed.ncbi.nlm.nih.gov/18533659/)
19. L. D. Lavis, Teaching old dyes new tricks: Biological probes built from fluoresceins and rhodamines. *Annu. Rev. Biochem.* **86**, 825–843 (2017). doi: [10.1146/annurev-biochem-061516-044839](https://doi.org/10.1146/annurev-biochem-061516-044839); pmid: [28399656](https://pubmed.ncbi.nlm.nih.gov/28399656/)
20. Y. Nasu, Y. Shen, L. Kramer, R. E. Campbell, Structure- and mechanism-guided design of single fluorescent protein-based biosensors. *Nat. Chem. Biol.* **17**, 509–518 (2021). doi: [10.1038/s41589-020-00718-x](https://doi.org/10.1038/s41589-020-00718-x); pmid: [33558715](https://pubmed.ncbi.nlm.nih.gov/33558715/)
21. L. Wang *et al.*, A general strategy to develop cell permeable and fluorogenic probes for multicolour nanoscopy. *Nat. Chem.* **12**, 165–172 (2020). doi: [10.1038/s41557-019-0371-1](https://doi.org/10.1038/s41557-019-0371-1); pmid: [31792385](https://pubmed.ncbi.nlm.nih.gov/31792385/)
22. J. B. Grimm *et al.*, A general method to optimize and functionalize red-shifted rhodamine dyes. *Nat. Methods* **17**, 815–821 (2020). doi: [10.1038/s41592-020-0909-6](https://doi.org/10.1038/s41592-020-0909-6); pmid: [32719532](https://pubmed.ncbi.nlm.nih.gov/32719532/)
23. C. Deo *et al.*, The HaloTag as a general scaffold for far-red tunable chemigenetic indicators. *Nat. Chem. Biol.* **17**, 718–723 (2021). doi: [10.1038/s41589-021-00775-w](https://doi.org/10.1038/s41589-021-00775-w); pmid: [33795886](https://pubmed.ncbi.nlm.nih.gov/33795886/)
24. L. Wang, J. Hiblot, C. Popp, L. Xue, K. Johansson, Environmentally sensitive color-shifting fluorophores for bioimaging. *Angew. Chem. Int. Ed.* **59**, 21880–21884 (2020). doi: [10.1002/anie.202008357](https://doi.org/10.1002/anie.202008357); pmid: [32762146](https://pubmed.ncbi.nlm.nih.gov/32762146/)
25. J. B. Grimm *et al.*, A general method to improve fluorophores for live-cell and single-molecule microscopy. *Nat. Methods* **12**, 244–250, 3, 250 (2015). doi: [10.1038/nmeth.3256](https://doi.org/10.1038/nmeth.3256); pmid: [25599551](https://pubmed.ncbi.nlm.nih.gov/25599551/)
26. J. B. Grimm *et al.*, A general method to fine-tune fluorophores for live-cell and in vivo imaging. *Nat. Methods* **14**, 987–994 (2017). doi: [10.1038/nmeth.4403](https://doi.org/10.1038/nmeth.4403); pmid: [28869757](https://pubmed.ncbi.nlm.nih.gov/28869757/)
27. G. Lukinavičius *et al.*, A near-infrared fluorophore for live-cell super-resolution microscopy of cellular proteins. *Nat. Chem.* **5**, 132–139 (2013). doi: [10.1038/nchem.1546](https://doi.org/10.1038/nchem.1546); pmid: [23344448](https://pubmed.ncbi.nlm.nih.gov/23344448/)
28. G. Lukinavičius *et al.*, Fluorogenic probes for multicolor imaging in living cells. *J. Am. Chem. Soc.* **138**, 9365–9368 (2016). doi: [10.1021/jacs.6b04782](https://doi.org/10.1021/jacs.6b04782); pmid: [27420907](https://pubmed.ncbi.nlm.nih.gov/27420907/)
29. Q. Zheng *et al.*, Rational design of fluorogenic and spontaneously blinking labels for super-resolution imaging. *ACS Cent. Sci.* **5**, 1602–1613 (2019). doi: [10.1021/acscentsci.9b00676](https://doi.org/10.1021/acscentsci.9b00676); pmid: [31572787](https://pubmed.ncbi.nlm.nih.gov/31572787/)
30. J. B. Grimm *et al.*, A general method to improve fluorophores using deuterated auxochromes. *JACS Au* **1**, 690–696 (2021). doi: [10.1021/jacsau.1c00006](https://doi.org/10.1021/jacsau.1c00006); pmid: [34056637](https://pubmed.ncbi.nlm.nih.gov/34056637/)
31. F. Deng *et al.*, Improved green and red GRAB sensors for monitoring spatiotemporal serotonin release in vivo. *Nat. Methods* **21**, 692–702 (2024). doi: [10.1038/s41592-024-02188-8](https://doi.org/10.1038/s41592-024-02188-8); pmid: [38443508](https://pubmed.ncbi.nlm.nih.gov/38443508/)
32. J. Feng *et al.*, Monitoring norepinephrine release in vivo using next-generation GRAB<sub>NE</sub> sensors. *Neuron* **112**, 1930–1942.e6 (2024). doi: [10.1016/j.neuron.2024.03.001](https://doi.org/10.1016/j.neuron.2024.03.001); pmid: [38547869](https://pubmed.ncbi.nlm.nih.gov/38547869/)
33. K. Z. Peters, E. B. Oleson, J. F. Cheer, A brain on cannabinoids: The role of dopamine release in reward seeking and addiction. *Cold Spring Harb. Perspect. Med.* **11**, a039305 (2021). doi: [10.1101/cshperspect.a039305](https://doi.org/10.1101/cshperspect.a039305); pmid: [31964646](https://pubmed.ncbi.nlm.nih.gov/31964646/)
34. S. Xie *et al.*, Red-shifted GRAB acetylcholine sensors for multiplex imaging in vivo. bioRxiv 627112 [Preprint] (2024); <https://doi.org/10.1101/2024.12.22.627112>.
35. A. Dong *et al.*, A fluorescent sensor for spatiotemporally resolved imaging of endocannabinoid dynamics in vivo. *Nat. Biotechnol.* **40**, 787–798 (2022). doi: [10.1038/s41587-021-01074-4](https://doi.org/10.1038/s41587-021-01074-4); pmid: [34764491](https://pubmed.ncbi.nlm.nih.gov/34764491/)
36. A. C. Kreitzer, W. G. Regehr, Retrograde inhibition of presynaptic calcium influx by endogenous cannabinoids at excitatory synapses onto Purkinje cells. *Neuron* **29**, 717–727 (2001). doi: [10.1016/S0896-6273\(01\)00246-X](https://doi.org/10.1016/S0896-6273(01)00246-X); pmid: [11301030](https://pubmed.ncbi.nlm.nih.gov/11301030/)
37. T. Ohno-Shosaku, T. Maejima, M. Kano, Endogenous cannabinoids mediate retrograde signals from depolarized postsynaptic neurons to presynaptic terminals. *Neuron* **29**, 729–738 (2001). doi: [10.1016/S0896-6273\(01\)00247-1](https://doi.org/10.1016/S0896-6273(01)00247-1); pmid: [11301031](https://pubmed.ncbi.nlm.nih.gov/11301031/)
38. R. I. Wilson, R. A. Nicoll, Endogenous cannabinoids mediate retrograde signalling at hippocampal synapses. *Nature* **410**, 588–592 (2001). doi: [10.1038/35069076](https://doi.org/10.1038/35069076); pmid: [11279497](https://pubmed.ncbi.nlm.nih.gov/11279497/)
39. R. Mechoulam, L. A. Parker, The endocannabinoid system and the brain. *Annu. Rev. Psychol.* **64**, 21–47 (2013). doi: [10.1146/annurev-psych-113011-143739](https://doi.org/10.1146/annurev-psych-113011-143739); pmid: [22804774](https://pubmed.ncbi.nlm.nih.gov/22804774/)
40. B. D. Heifets, P. E. Castillo, Endocannabinoid signaling and long-term synaptic plasticity. *Annu. Rev. Physiol.* **71**, 283–306 (2009). doi: [10.1146/annurev.physiol.010908.163149](https://doi.org/10.1146/annurev.physiol.010908.163149); pmid: [19575681](https://pubmed.ncbi.nlm.nih.gov/19575681/)
41. C. Liu, P. Gosh, P. S. Kaeser, Spatial and temporal scales of dopamine transmission. *Nat. Rev. Neurosci.* **22**, 345–358 (2021). doi: [10.1038/s41583-021-00455-7](https://doi.org/10.1038/s41583-021-00455-7); pmid: [33837376](https://pubmed.ncbi.nlm.nih.gov/33837376/)
42. M. Sarter, V. Parikh, W. M. Howe, Phasic acetylcholine release and the volume transmission hypothesis: Time to move on. *Nat. Rev. Neurosci.* **10**, 383–390 (2009). doi: [10.1038/nrn2635](https://doi.org/10.1038/nrn2635); pmid: [19377503](https://pubmed.ncbi.nlm.nih.gov/19377503/)
43. N. Chuhma, S. Mingote, H. Moore, S. Rayport, Dopamine neurons control striatal cholinergic neurons through regionally heterogeneous dopamine and glutamate signaling. *Neuron* **81**, 901–912 (2014). doi: [10.1016/j.neuron.2013.12.027](https://doi.org/10.1016/j.neuron.2013.12.027); pmid: [24559678](https://pubmed.ncbi.nlm.nih.gov/24559678/)
44. C. Straub, N. X. Tritsch, N. A. Hagan, C. Gu, B. L. Sabatini, Multiphasic modulation of cholinergic interneurons by nigrostriatal afferents. *J. Neurosci.* **34**, 8557–8569 (2014). doi: [10.1523/JNEUROSCI.0589-14.2014](https://doi.org/10.1523/JNEUROSCI.0589-14.2014); pmid: [24948810](https://pubmed.ncbi.nlm.nih.gov/24948810/)
45. S. Wieland *et al.*, Phasic dopaminergic activity exerts fast control of cholinergic interneuron firing through sequential NMDA, D2, and D1 receptor activation. *J. Neurosci.* **34**, 11549–11559 (2014). doi: [10.1523/JNEUROSCI.1175-14.2014](https://doi.org/10.1523/JNEUROSCI.1175-14.2014); pmid: [25164653](https://pubmed.ncbi.nlm.nih.gov/25164653/)
46. C. Liu *et al.*, An action potential initiation mechanism in distal axons for the control of dopamine release. *Science* **375**, 1378–1385 (2022). doi: [10.1126/science.abn0532](https://doi.org/10.1126/science.abn0532); pmid: [35324301](https://pubmed.ncbi.nlm.nih.gov/35324301/)
47. F.-M. Zhou, Y. Liang, J. A. Dani, Endogenous nicotinic cholinergic activity regulates dopamine release in the striatum. *Nat. Neurosci.* **4**, 1224–1229 (2001). doi: [10.1038/nn769](https://doi.org/10.1038/nn769); pmid: [11713470](https://pubmed.ncbi.nlm.nih.gov/11713470/)
48. S. Threlfell *et al.*, Striatal dopamine release is triggered by synchronized activity in cholinergic interneurons. *Neuron* **75**, 58–64 (2012). doi: [10.1016/j.neuron.2012.04.038](https://doi.org/10.1016/j.neuron.2012.04.038); pmid: [22794260](https://pubmed.ncbi.nlm.nih.gov/22794260/)
49. Z. Wu *et al.*, A sensitive GRAB sensor for detecting extracellular ATP in vitro and in vivo. *Neuron* **110**, 770–782.e5 (2022). doi: [10.1016/j.neuron.2021.11.027](https://doi.org/10.1016/j.neuron.2021.11.027); pmid: [34942116](https://pubmed.ncbi.nlm.nih.gov/34942116/)
50. B. Mohar *et al.*, DELTA: A method for brain-wide measurement of synaptic protein turnover reveals localized plasticity during learning. *Nat. Neurosci.* **28**, 1089–1098 (2025). doi: [10.1038/s41593-025-01923-4](https://doi.org/10.1038/s41593-025-01923-4); pmid: [40164741](https://pubmed.ncbi.nlm.nih.gov/40164741/)
51. E. Bulovaite *et al.*, A brain atlas of synapse protein lifetime across the mouse lifespan. *Neuron* **110**, 4057–4073.e8 (2022). doi: [10.1016/j.neuron.2022.09.009](https://doi.org/10.1016/j.neuron.2022.09.009); pmid: [36202095](https://pubmed.ncbi.nlm.nih.gov/36202095/)
52. K. Yamaguchi, S. Inoue, O. Ohara, T. Nagase, “Pulse-chase experiment for the analysis of protein stability in cultured mammalian cells by covalent fluorescent labeling of fusion proteins” in *Reverse Chemical Genetics*, H. Koga, Ed. (Humana Press, 2009), pp. 121–131. doi: [10.1007/978-1-60761-232-2\\_10](https://doi.org/10.1007/978-1-60761-232-2_10)
53. K. T. Beier *et al.*, Circuit architecture of VTA dopamine neurons revealed by systematic input-output mapping. *Cell* **162**, 622–634 (2015). doi: [10.1016/j.cell.2015.07.015](https://doi.org/10.1016/j.cell.2015.07.015); pmid: [26232228](https://pubmed.ncbi.nlm.nih.gov/26232228/)
54. K. Abe *et al.*, Functional diversity of dopamine axons in prefrontal cortex during classical conditioning. *eLife* **12**, RP91136 (2024). doi: [10.7554/eLife.91136.3](https://doi.org/10.7554/eLife.91136.3); pmid: [38747563](https://pubmed.ncbi.nlm.nih.gov/38747563/)
55. R. A. Phillips III *et al.*, An atlas of transcriptionally defined cell populations in the rat ventral tegmental area. *Cell Rep.* **39**, 110616 (2022). doi: [10.1016/j.celrep.2022.110616](https://doi.org/10.1016/j.celrep.2022.110616); pmid: [35385745](https://pubmed.ncbi.nlm.nih.gov/35385745/)

56. B. Yaghmaeian Salmani *et al.*, Transcriptomic atlas of midbrain dopamine neurons uncovers differential vulnerability in a parkinsonism lesion model. *eLife* **12**, RP89482 (2024). doi: [10.7554/eLife.89482.3](https://doi.org/10.7554/eLife.89482.3); pmid: [38587883](https://pubmed.ncbi.nlm.nih.gov/38587883/)
57. E. Casey, M. E. Avale, A. Kravitz, M. Rubinstein, Dopaminergic innervation at the central nucleus of the amygdala reveals distinct topographically segregated regions. *Brain Struct. Funct.* **228**, 663–675 (2023). doi: [10.1007/s00429-023-02614-1](https://doi.org/10.1007/s00429-023-02614-1); pmid: [36737539](https://pubmed.ncbi.nlm.nih.gov/36737539/)
58. E. Casey, M. E. Avale, A. Kravitz, M. Rubinstein, Partial ablation of postsynaptic dopamine D2 receptors in the central nucleus of the amygdala increases risk avoidance in exploratory tasks. *eNeuro* **9**, ENEURO.528-21.2022 (2022). doi: [10.1523/ENEURO.0528-21.2022](https://doi.org/10.1523/ENEURO.0528-21.2022); pmid: [35210287](https://pubmed.ncbi.nlm.nih.gov/35210287/)
59. E. J. Nunes, N. A. Addy, P. J. Conn, D. J. Foster, Targeting the actions of muscarinic receptors on dopamine systems: New strategies for treating neuropsychiatric disorders. *Annu. Rev. Pharmacol. Toxicol.* **64**, 277–289 (2024). doi: [10.1146/annurev-pharmtox-051921-023858](https://doi.org/10.1146/annurev-pharmtox-051921-023858); pmid: [37552895](https://pubmed.ncbi.nlm.nih.gov/37552895/)
60. S. E. Yohn, P. J. Weiden, C. C. Felder, S. M. Stahl, Muscarinic acetylcholine receptors for psychotic disorders: Bench-side to clinic. *Trends Pharmacol. Sci.* **43**, 1098–1112 (2022). doi: [10.1016/j.tips.2022.09.006](https://doi.org/10.1016/j.tips.2022.09.006); pmid: [36273943](https://pubmed.ncbi.nlm.nih.gov/36273943/)
61. A. G. Nair *et al.*, The high efficacy of muscarinic M4 receptor in D1 medium spiny neurons reverses striatal hyperdopaminergia. *Neuropharmacology* **146**, 74–83 (2019). doi: [10.1016/j.neuropharm.2018.11.029](https://doi.org/10.1016/j.neuropharm.2018.11.029); pmid: [30468798](https://pubmed.ncbi.nlm.nih.gov/30468798/)
62. N. J. Bruce *et al.*, Regulation of adenylyl cyclase 5 in striatal neurons confers the ability to detect coincident neuromodulatory signals. *PLoS Comput. Biol.* **15**, e1007382 (2019). doi: [10.1371/journal.pcbi.1007382](https://doi.org/10.1371/journal.pcbi.1007382); pmid: [31665146](https://pubmed.ncbi.nlm.nih.gov/31665146/)
63. W. Shen *et al.*, M4 muscarinic receptor signaling ameliorates striatal plasticity deficits in models of L-DOPA-induced dyskinesia. *Neuron* **88**, 762–773 (2015). doi: [10.1016/j.neuron.2015.10.039](https://doi.org/10.1016/j.neuron.2015.10.039); pmid: [26590347](https://pubmed.ncbi.nlm.nih.gov/26590347/)
64. L. Chantranupong *et al.*, Dopamine and glutamate regulate striatal acetylcholine in decision-making. *Nature* **621**, 577–585 (2023). doi: [10.1038/s41586-023-06492-9](https://doi.org/10.1038/s41586-023-06492-9); pmid: [37557915](https://pubmed.ncbi.nlm.nih.gov/37557915/)
65. A. C. Krok *et al.*, Intrinsic dopamine and acetylcholine dynamics in the striatum of mice. *Nature* **621**, 543–549 (2023). doi: [10.1038/s41586-023-05995-9](https://doi.org/10.1038/s41586-023-05995-9); pmid: [37558873](https://pubmed.ncbi.nlm.nih.gov/37558873/)
66. L. Wang *et al.*, A high-performance genetically encoded fluorescent indicator for in vivo cAMP imaging. *Nat. Commun.* **13**, 5363 (2022). doi: [10.1038/s41467-022-32994-7](https://doi.org/10.1038/s41467-022-32994-7); pmid: [36097007](https://pubmed.ncbi.nlm.nih.gov/36097007/)
67. W. Liu, C. Liu, P.-G. Ren, J. Chu, L. Wang, An improved genetically encoded fluorescent cAMP indicator for sensitive cAMP imaging and fast drug screening. *Front. Pharmacol.* **13**, 902290 (2022). doi: [10.3389/fphar.2022.902290](https://doi.org/10.3389/fphar.2022.902290); pmid: [35694242](https://pubmed.ncbi.nlm.nih.gov/35694242/)
68. Y. Zheng, Y. Li, Past, present, and future of tools for dopamine detection. *Neuroscience* **525**, 13–25 (2023). doi: [10.1016/j.neuroscience.2023.06.025](https://doi.org/10.1016/j.neuroscience.2023.06.025); pmid: [37419404](https://pubmed.ncbi.nlm.nih.gov/37419404/)
69. D. Hilger, M. Masureel, B. K. Kobilka, Structure and dynamics of GPCR signaling complexes. *Nat. Struct. Mol. Biol.* **25**, 4–12 (2018). doi: [10.1038/s41594-017-0011-7](https://doi.org/10.1038/s41594-017-0011-7); pmid: [29323277](https://pubmed.ncbi.nlm.nih.gov/29323277/)
70. B. T. DeVree *et al.*, Allosteric coupling from G protein to the agonist-binding pocket in GPCRs. *Nature* **535**, 182–186 (2016). doi: [10.1038/nature18324](https://doi.org/10.1038/nature18324); pmid: [27362234](https://pubmed.ncbi.nlm.nih.gov/27362234/)
71. P. J. Conn, A. Christopoulos, C. W. Lindsley, Allosteric modulators of GPCRs: A novel approach for the treatment of CNS disorders. *Nat. Rev. Drug Discov.* **8**, 41–54 (2009). doi: [10.1038/nrd2760](https://doi.org/10.1038/nrd2760); pmid: [19116626](https://pubmed.ncbi.nlm.nih.gov/19116626/)
72. A. S. Abdelfattah *et al.*, Sensitivity optimization of a rhodopsin-based fluorescent voltage indicator. *Neuron* **111**, 1547–1563.e9 (2023). doi: [10.1016/j.neuron.2023.03.009](https://doi.org/10.1016/j.neuron.2023.03.009); pmid: [37015225](https://pubmed.ncbi.nlm.nih.gov/37015225/)
73. A. S. Abdelfattah *et al.*, Bright and photostable chemigenetic indicators for extended in vivo voltage imaging. *Science* **365**, 699–704 (2019). doi: [10.1126/science.aav6416](https://doi.org/10.1126/science.aav6416); pmid: [31371562](https://pubmed.ncbi.nlm.nih.gov/31371562/)
74. H. Farrants *et al.*, A modular chemigenetic calcium indicator for multiplexed in vivo functional imaging. *Nat. Methods* **21**, 1916–1925 (2024). doi: [10.1038/s41592-024-02411-6](https://doi.org/10.1038/s41592-024-02411-6); pmid: [39304767](https://pubmed.ncbi.nlm.nih.gov/39304767/)
75. S. Nonomura *et al.*, Monitoring and updating of action selection for goal-directed behavior through the striatal direct and indirect pathways. *Neuron* **99**, 1302–1314.e5 (2018). doi: [10.1016/j.neuron.2018.08.002](https://doi.org/10.1016/j.neuron.2018.08.002); pmid: [30146299](https://pubmed.ncbi.nlm.nih.gov/30146299/)
76. J. Jeon *et al.*, A subpopulation of neuronal M<sub>4</sub> muscarinic acetylcholine receptors plays a critical role in modulating dopamine-dependent behaviors. *J. Neurosci.* **30**, 2396–2405 (2010). doi: [10.1523/JNEUROSCI.3843-09.2010](https://doi.org/10.1523/JNEUROSCI.3843-09.2010); pmid: [20147565](https://pubmed.ncbi.nlm.nih.gov/20147565/)
77. W. Wu *et al.*, 2X-rhodamine: A bright and fluorogenic scaffold for developing near-infrared chemigenetic indicators. *J. Am. Chem. Soc.* **146**, jacs.4c03485 (2024). doi: [10.1021/jacs.4c03485](https://doi.org/10.1021/jacs.4c03485); pmid: [38605649](https://pubmed.ncbi.nlm.nih.gov/38605649/)
78. A. Keppler *et al.*, A general method for the covalent labeling of fusion proteins with small molecules in vivo. *Nat. Biotechnol.* **21**, 86–89 (2003). doi: [10.1038/nbt765](https://doi.org/10.1038/nbt765); pmid: [12469133](https://pubmed.ncbi.nlm.nih.gov/12469133/)
79. J. Mo *et al.*, Third-generation covalent TMP-tag for fast labeling and multiplexed imaging of cellular proteins. *Angew. Chem. Int. Ed.* **61**, e202207905 (2022). doi: [10.1002/anie.202207905](https://doi.org/10.1002/anie.202207905); pmid: [35816052](https://pubmed.ncbi.nlm.nih.gov/35816052/)

## ACKNOWLEDGMENTS

We thank Y. Rao for providing the upright confocal microscope; the optical imaging platform and small animal imaging platform of the National Center for Protein Sciences at Peking University in Beijing, China, for their support and assistance with the Operetta CLS high-content imaging system, the Nikon A1RSi+ laser scanning microscope, and the behavior facility; the Laboratory Animal Center of Peking University for advice and technical support; Thinker Tech Nanjing BioScience for its customization and assistance with the fiber photometry system; and members of the Li lab for helpful suggestions and comments regarding the manuscript. Some diagrams were created using BioRender.com. **Funding:** This work was supported by the Beijing Municipal Science and Technology Commission (grant Z220009 to Y.L.), the National Natural Science Foundation of China (grant 32525003 to Y.L.), the National Key R&D Program of China (grants 2022YFE0108700 and 2023YFE0207100 to Y.L.), the National Institutes of Health BRAIN Initiative (grant 1U01NS120824 to Y.L.), the Creative Research Groups of the National Natural Science Foundation of China (grant 32321003 to Y.M.), the National Science and Technology Innovation 2030 Major Program (grant 2021ZD0204502 to Y.M.), the Beijing National Laboratory for Molecular Sciences (grant BNLS202407 to Z.C.), and the International Cooperation and Exchange of the National Natural Science Foundation of China (grant W2412031 to Z.C.). Support was also provided by the Peking-Tsinghua Center for Life Sciences, the State Key Laboratory of Membrane Biology at Peking University School of Life Sciences, the Feng Foundation of Biomedical Research (Y.L.), and the New Cornerstone Science Foundation through the New Cornerstone Investigator Program (Y.L.). **Author contributions:** Y.L. supervised the project. Y. Zheng and Y.L. designed the study. Y. Zheng developed and optimized the sensors. Y. Zheng performed the experiments related to characterizing the sensors with help from Y. Zhang, G.L., Z.W., Y. Zhuo, F.D., E.J., Y.Y., H.H., and K.Z. R.C. performed the confocal imaging of acute brain slices. K.W., S.F., and X.Z. performed the zebrafish imaging under the supervision of Y.M. Y. Zheng performed the fiber photometry recording experiments with help from H.D., Y.W., Y.C., J.W., X.M., and S.L. J.Z. performed the chemical conjugation of the HaloTag ligand to chemical dyes under the supervision of Z.C. J.B.G. and L.D.L. provided the JF dyes, and K.J. provided other dyes. K.J. and E.R.S. provided assistance with the chemigenetic strategy. All authors contributed to the interpretation and analysis of the data. Y. Zheng and Y.L. wrote the manuscript with input from all coauthors. **Competing interests:** L.D.L. and J.B.G. are inventors on patents held by HHMI, including “Azetidine-substituted fluorescent compounds” (US 9933417), “Deuterated fluorophores” (US 11787946), and a patent application titled “Red-shifted fluorophores” (US 2021/0171490). These patents cover azetidine-containing, deuterated, and fluorinated rhodamine dyes. **Data and materials availability:** DNA plasmids of HaloDA1.0 and HaloDAmut sensors used in this study have been deposited to Addgene (234408-234411). All other data needed to evaluate the conclusions in this study are available in the main text or the supplementary materials. **License information:** Copyright © 2025 the authors, some rights reserved; exclusive licensee American Association for the Advancement of Science. No claim to original US government works. <https://www.science.org/about/science-licenses-journal-article-reuse>

## SUPPLEMENTARY MATERIALS

[science.org/doi/10.1126/science.adt7705](https://science.org/doi/10.1126/science.adt7705)  
Materials and Methods; Figs. S1 to S15; References (80–83); MDAR Reproducibility Checklist  
Submitted 10 October 2024; accepted 20 March 2025

10.1126/science.adt7705